Localized blood–brain barrier opening in infiltrating gliomas with MRI-guided acoustic emissions–controlled focused ultrasound

Pavlos Anastasiadis[a,b], Dheeraj Gandhi[c], Yutong Guo[d], Abdul-Kareem Ahmed[a], Soren M. Bentzen[b,e,f], Costas Arvanitis[d,g], and Graeme F. Woodworth[a,b,c,1]

[a]Department of Neurosurgery, University of Maryland School of Medicine, Baltimore, MD 21201; [b]Experimental Therapeutics Program & Brain Tumor Treatment and Research Center, University of Maryland Marlene and Stewart Greenebaum Comprehensive Cancer Center, Baltimore, MD 21201; [c]Department of Diagnostic Radiology and Nuclear Medicine, University of Maryland School of Medicine, Baltimore, MD 21201; [d]School of Mechanical Engineering, Georgia Institute of Technology, Atlanta, GA 30332; [e]Epidemiology & Public Health, University of Maryland, Baltimore, MD 21201; [f]Radiation Oncology, University of Maryland, Baltimore, MD 21201; and [g]Department of Biomedical Engineering, Georgia Institute of Technology and Emory University, Atlanta, GA 30332

Edited by Henry Brem, Johns Hopkins University, Baltimore, MD, and accepted by Editorial Board Member Jeremy Nathans July 19, 2021 (received for review April 8, 2021)

Pharmacological treatment of gliomas and other brain-infiltrating tumors remains challenging due to limited delivery of most therapeutics across the blood–brain barrier (BBB). Transcranial MRI-guided focused ultrasound (FUS), an emerging technology for noninvasive brain treatments, enables transient opening of the BBB through acoustic activation of circulating microbubbles. Here, we evaluate the safety and utility of transcranial microbubble-enhanced FUS (MB-FUS) for spatially targeted BBB opening in patients with infiltrating gliomas. In this Phase 0 clinical trial (NCT03322813), we conducted comparative and quantitative analyses of FUS exposures (sonications) and their effects on gliomas using MRI, histopathology, microbubble acoustic emissions (harmonic dose [HD]), and fluorescence-guided surgery metrics. Contrast-enhanced MRI and histopathology indicated safe and reproducible BBB opening in all patients. These observations occurred using a power cycling closed feedback loop controller, with the power varying by nearly an order of magnitude on average. This range underscores the need for monitoring and titrating the exposure on a patient-by-patient basis. We found a positive correlation between microbubble acoustic emissions (HD) and MR-evident BBB opening ($P = 0.07$) and associated interstitial changes ($P < 0.01$), demonstrating the unique capability to titrate the MB-FUS effects in gliomas. Importantly, we identified a 2.2-fold increase of fluorescein accumulation in MB-FUS–treated compared to untreated nonenhancing tumor tissues ($P < 0.01$) while accounting for vascular density. Collectively, this study demonstrates the capabilities of MB-FUS for safe, localized, controlled BBB opening and highlights the potential of this technology to improve the surgical and pharmacologic treatment of brain tumors.

focused ultrasound | blood–brain barrier | glioma | microbubbles | acoustic emissions

The blood–brain barrier (BBB) is composed of neurovascular units with contributions from endothelial cells, pericytes, astrocytes, and neurons that together control the trafficking of metabolites, signaling molecules, toxins, pathogens, and most drugs between the bloodstream and central nervous system (CNS) (1, 2). Thus, the BBB effectively limits pharmacologic treatment of numerous CNS diseases, including infiltrating gliomas, which diffusely invade the brain (3). Glioblastoma (GBM, grade IV glioma), a particularly aggressive and invasive form of brain cancer, is associated with a grim prognosis in part due to the lack of permeability of the BBB to otherwise promising therapeutics (4, 5). This vexing challenge of limited drug delivery across the BBB in infiltrating gliomas motivated the work described here. To date, there are no methods for effective, noninvasive, and safe BBB opening (BBBO) with the potential for spatiotemporal control of localized drug delivery in brain tumors (3, 6–9).

Focused ultrasound (FUS) is an emerging technology capable of noninvasively delivering acoustic energy into tissues throughout the body (10). Modern FUS systems include devices that can activate circulating microbubbles (MBs) to create temporary BBBO through the intact skull. The ExAblate Neuro system (InSightec Ltd.) and the NaviFUS system are both devices for use through the intact skull (11–13). The ExAblate MRI-guided FUS (MRgFUS) system consists of a high-field MRI scanner, a hemispheric 1,024-element phased array ultrasound transducer interfaced with computer systems to align, steer, and control the transducer array utilizing skull data from a computed tomography (CT) scan (Fig. 1). While fundamentally different from this approach, we note that implantable systems offer yet another method of achieving BBBO in the clinical realm. The SonoCloud low-intensity contact ultrasound system (CarThera) is composed of an implantable transducer that secures to the skull following craniotomy and can be accessed percutaneously over multiple sessions (14, 15). Regardless of the FUS approach used, whether through the intact skull or following cranial transducer implantation, in this context, BBBO is achieved as a result of the interaction between the acoustic energy field and circulating MBs that are administered intravenously.

Significance

The blood–brain barrier (BBB) is a critical obstacle to delivering most therapeutics into the brain. In this study, we report combined MRI, histological, and real-time acoustic emissions monitoring findings from a Phase 0 clinical trial examining microbubble-enhanced transcranial focused ultrasound for controlled BBB opening in patients with infiltrating gliomas. The data revealed the capability of this technology to provide safe, controlled, and tightly monitored BBB opening through the intact skull. Our findings demonstrate the capability of this technology to tune BBB opening in real-time, creating opportunities for improved treatment of brain tumors.

Author contributions: G.F.W. designed research; P.A., D.G., Y.G., A.-K.A., C.A., and G.F.W. performed research; P.A., D.G., Y.G., C.A., and G.F.W. contributed new reagents/analytic tools; P.A., D.G., Y.G., A.-K.A., S.M.B., C.A., and G.F.W. analyzed data; and P.A., S.M.B., C.A., and G.F.W. wrote the paper.

The authors declare no competing interest.

This article is a PNAS Direct Submission. H.B. is a guest editor invited by the Editorial Board.

[1]To whom correspondence may be addressed. Email: gwoodworth@som.umaryland.edu.

This article contains supporting information online at https://www.pnas.org/lookup/suppl/doi:10.1073/pnas.2103280118/-/DCSupplemental.

Published September 9, 2021.

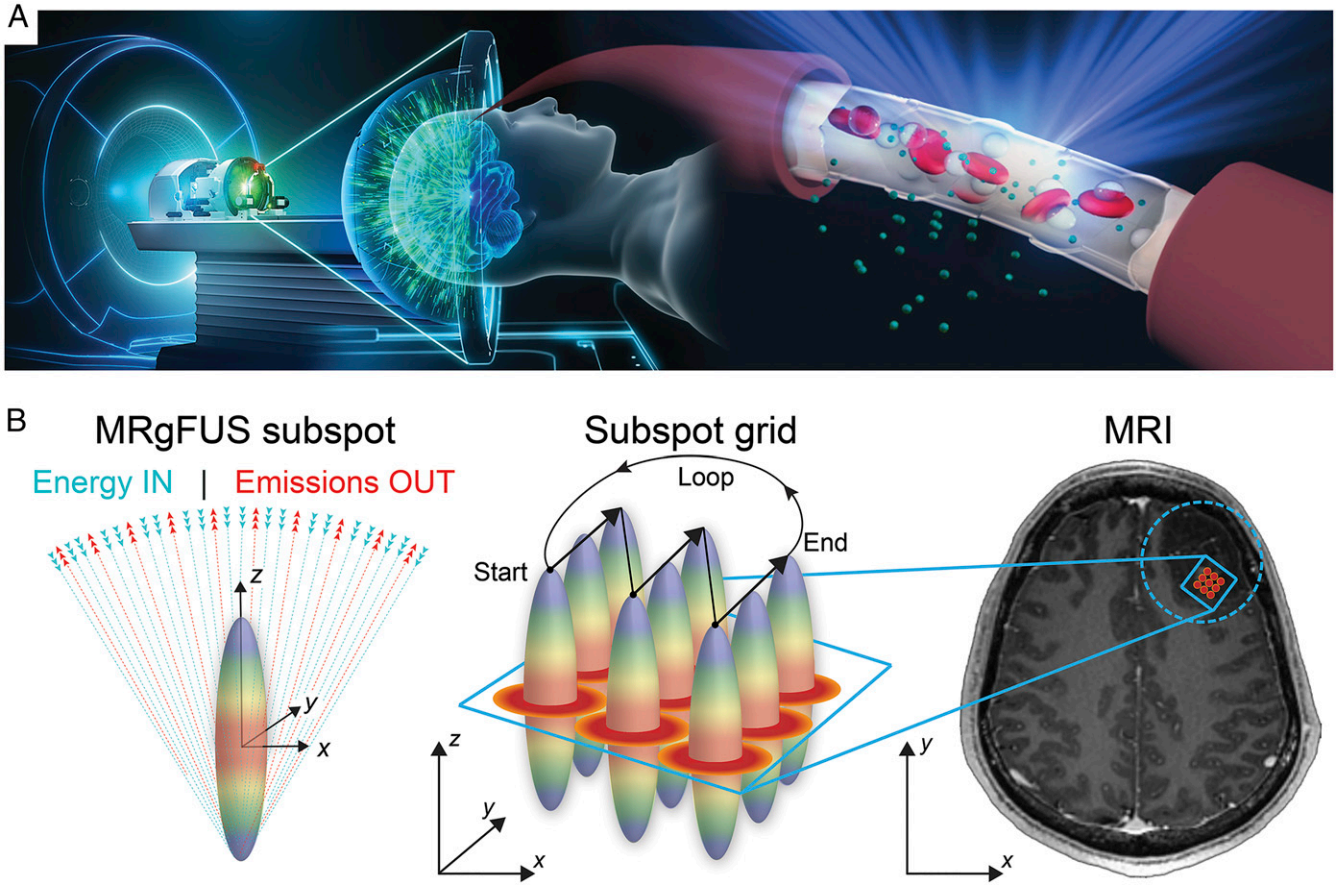

Fig. 1. MRgFUS-mediated BBBO: (*A*) Schematic illustration of the transcranial MRgFUS system. The helmet-shaped hemispherical phased array is comprised of 1,024 ultrasound transducers allowing for electronic steering and beam refocusing through the skull. Intracerebral endothelial cells are shown as FUS beams converge toward the target location causing circulating MBs within the acoustic field to oscillate. The resulting stable MB oscillation leads to BBBO. (*B*, *Left*) Schematic illustration of the focal spot for an ideal hemispherical phased array as ultrasound beams emanating from the phased array converge forming a theoretical ovoid geometry. The length of the focal spot corresponds to one wavelength along the *z*-axis and half a wavelength in the *XY*-plane. At 230 kHz—the center frequency used for BBBO—one wavelength corresponds to ~6.5 mm. (*Middle*) Depiction of the subspot grid encompassing nine individual subspots. Focal spots (gradient disks) are shown across the 3 × 3 subspot grid. The arrows indicate the direction of the ultrasound beam steering pattern during sonications, which proceeded in a linear loop pattern. (*Right*) Axial T1w MR image showing the subspot grid target in two dimensions within the tumor region (enclosed dotted circle). The arrows in the *XY*-plane indicate the beam steering direction during treatment.

Three notable enabling technologies have propelled the translation of MB-enhanced FUS (MB-FUS) systems and treatment methodologies and serve as the foundation for this work: 1) advanced image-guidance platforms; 2) computer-controlled refocusing (or aberration correction) of multielement transducer arrays; and 3) real-time acoustic emissions monitoring (AEM) technologies for closed-feedback loop control of MB-FUS effects. For thermo-ablative applications of MRgFUS, similar advancements in image guidance, acoustic energy control, and real-time monitoring of FUS effects (e.g., MR thermometry), led to Food and Drug Administration (FDA) approval of this new treatment device (11, 16).

The development of such closed feedback loops (CFLs) during FUS treatments has set the foundation for safety monitoring and treatment control during intracranial applications. The CFL systems provide information to adjust ultrasound parameters (e.g., power) and targeting while gauging for undesirable effects (e.g., bubble collapse and/or tissue damage) (17, 18). In MB-FUS, the MBs are activated within the FUS acoustic energy field, leading to oscillations in relation to the FUS frequency (typically in kilohertz) and power (typically in milliwatts). As the FUS power increases, the MBs oscillate in an increasingly nonlinear manner, thereby generating acoustic emissions with specific bands relative to the baseline frequency (e.g., fundamental), termed "harmonics." The harmonic signals can be detected and measured using integrated acoustic emissions detectors (e.g., hydrophones) (19). Stable oscillations have a characteristic harmonic pattern that differentiates the MB-FUS effects from those associated with tissue resonances or unstable MB oscillations that are associated with bubble collapse and potential injury. By recording and measuring the AEM data during MB-FUS treatments, harmonic data can be recorded in real-time and used to calculate "harmonic doses" (HD), which can be prescribed to specific targets. Accordingly, the incorporation of AEM into CFL monitoring and control systems (analogous to MR thermometry in thermo-ablative applications) introduce real-time power cycling, safety threshold monitoring, and tightly controlled and prescriptive MB-FUS treatments (20–24).

These capabilities to control and monitor FUS have led to the ongoing advancement of FUS-mediated BBBO in human patients for the treatment of brain tumors and Alzheimer's disease (25–28). The availability of clinical-grade MBs, originally developed as blood pool contrast agents (29, 30), has accelerated clinical applications of MB-FUS BBBO, leading to multiple ongoing clinical trials in the United States (e.g., NCT03322813, NCT03551249, NCT04417088, and NCT04667715).

Despite these ongoing studies and clinical stage components, there is a lack of cross-referenced imaging, intraoperative, histological, and ultrasound parameters, including AEM data, from FUS-treated patients. Such data and related analyses will not only assess the robustness of the proposed methods but also provide evidence to refine these methods and our understanding of the role of MB-FUS in controlling drug delivery across the BBB in patients with infiltrating gliomas.

In this study, we explored transcranial MB-FUS for localized BBBO in patients with intrinsic brain tumors (grade II and III infiltrating gliomas) prior to planned surgical resections. More specifically, the primary aim of this study was to assess the safety and feasibility of MB-FUS for BBBO in nonenhancing regions of infiltrating gliomas given that BBB in tumor-infiltrated brain regions—where most infiltrating gliomas "hide" escaping removal or other treatments—remains largely intact. Secondarily, we sought to analyze stereotactically localized FUS-treated tissues to correlate the intraoperative, histopathological, MRI, and AEM findings. We report combined correlative and quantitative analyses of patient datasets from MB-FUS treatments of intrinsic brain tumors and demonstrate the capability of MB-FUS to both increase and localize the delivery of circulating agents into targeted brain tumor regions with a high degree of spatiotemporal control. We also demonstrate that localized extravasation of fluorescent dye offers the potential to improve surgical visibility, thereby enabling a promising intraoperative approach, which leverages this technology and its capabilities to visually enhance regions of a planned surgical resection volumes. Taken together, these findings and results present intriguing opportunities to improve the surgical and pharmacologic treatment of patients with infiltrating gliomas and other brain diseases.

Results

Study Design and Patient Cohort Data. The primary study outcome measure was the occurrence of device- (e.g., ExAblate Neuro Type 2) and procedure-related (e.g., BBBO) adverse events during sonications. The secondary study outcome measures were metrics to assess the feasibility of BBBO in infiltrating gliomas. The extent of BBBO were determined by the degree and volume of MB-FUS–mediated contrast-enhancement. Of the seven patients screened for the study, four patients met the inclusion/exclusion criteria and enrolled to participate. The mean age of the study participants was 32.5 y (range: 29 to 36) at the time of MRgFUS treatment and surgery. The subjects were all neurologically intact prior to surgery, and each had a Karnofsky performance score (KPS) of above 80. The primary presenting symptom was a seizure in three of the four patients. The tumors were all located in the frontal or temporal lobes and had a mean volume of 18.2 cm^3 at the time of diagnosis. Two of the four patients had tumors with some intrinsic contrast-enhancement on pretreatment MRI. A representative patient MRI before FUS treatment is shown in Fig. 2*A*, demonstrating a right frontal intrinsic brain tumor with minimal intrinsic contrast-enhancement and T2 hyperintense signal. Following FUS treatment, new contrast-enhancement was visualized within the targeted region of the planned surgical resection volume (Fig. 2*B*). During fluorescein-enhanced surgical resection, the FUS-targeted region corresponding to the new area of contrast-enhancement was clearly visualized using the Zeiss YELLOW 560 module on the operative microscope (OPMI Pentero, Carl Zeiss) (Fig. 2*C*). All patients underwent surgery following MRgFUS treatments and had gross total resection of the contrast-enhancing and T2 hyperintense tumor components (Fig. 2*D*). A timeline schematic showing the intervals between MB-FUS and post-FUS MRI (32 to 65 min), between post-FUS MRI and fluorescein injection (154 to 203 min), and between fluorescein injection and tissue resection (45 to 65 min) is shown in *SI Appendix*, Fig. S1. Histopathological analyses demonstrated one diffuse infiltrating glioma (World Health Organization [WHO] Grade II) and three oligodendrogliomas, one WHO Grade II, and two anaplastic WHO Grade III (Table 1). There were no serious adverse events in this study, including neurological deficits or clinical seizure activity detected in the patients following surgery. With a sample size of four patients, the upper limit of the exact binomial one-sided 95% CI is 0.527, and for a one-sided 90% CI the upper limit is 0.438. Thus, with the current sample size, we can rule out that the incidence of even low-grade adverse events is excessive. All patients were discharged to home after an average of 2.75 (± SD 0.83) days stay in the hospital. Median follow-up time at the time of this publication was 15.7 mo, with no evidence of tumor recurrence in all four cases.

FUS BBBO Treatments. All patients underwent MB-FUS–mediated BBBO under MR image guidance without detectable adverse events by both clinical and radiologic examinations. The FUS targeting grid ranged from 9 to 31 subspots. For the first three patients, treatment volume was an average of 0.57 cm^3; in the fourth patient, the system controller and software were updated to enable larger, volumetric targeting, resulting in a treatment volume of 10.08 cm^3. The acoustic energy was sequentially titrated by incrementally increasing power until the onset of subharmonic emissions as recorded in real-time by an array of eight hydrophones integrated inside the acoustic helmet. Each brief sonication was then adjusted to 50% of that power threshold. This approach is based on previously reported observations that sonications conducted at 50% of the pressure threshold where subharmonic activity is detected result in safe BBBO without evidence of tissue damage (21). The average power throughout each patient treatment ranged between 3.38 W and 24.55 W, with the maximum sonication power being 47.27 Watts (Table 2). This broad range of exposures (an order of magnitude) underscores the need for monitoring and titrating the exposure on a patient-by-patient basis.

The accumulated mechanical energy within the targeting subspot grid was recorded during the treatments in real-time based on AEM data. The colorimetric energy maps of the accumulated recorded mechanical energy within the targeting subspot grid revealed variations within the target regions and new areas of contrast-enhancement on the posttreatment MRI. The new enhancement corresponded to higher subharmonic levels of acoustic emissions (Fig. 3). The data were derived from the Fast Fourier Transform of the emissions recorded by the system's hydrophones (*SI Appendix*, Fig. S2). The overlaid treatment region denoting the target subspots and the corresponding energy maps indicate the deposition of acoustic energy and the resulting MB-FUS–derived enhancement in the post-FUS contrast-enhanced T1-weighted (T1c) MR images compared to contrast-enhanced MRI acquisitions during treatment planning (pre-FUS). Together, these data highlight the importance of AEM for monitoring and titrating the FUS exposure both within and across different tumors.

Comparative Analysis of Fluorescein in Intrinsically Enhancing, Nonenhancing, and FUS-Treated Tumor Regions. To directly test the capability of MB-FUS to promote the localized delivery of circulating agents into targeted brain regions, the delivery of fluorescein (molecular weight: 376 g/mol) was assessed in tumor tissues with intrinsic contrast-enhancement, no contrast-enhancement, and MB-FUS–mediated contrast-enhancement. Intensity-based fluorescence signal quantification of the excised brain tissues revealed a higher fluorescein accumulation in tumor tissues with intrinsic contrast-enhancement compared to the regions with no contrast-enhancement (Fig. 4 *A*, *B*, and *D*). Interestingly, we found a 2.2-fold increase of fluorescein accumulation in MB-FUS–treated compared to untreated nonenhancing tumor tissues ($P < 0.01$) (Fig. 4). CD31 labeling (Fig. 4*E*) indicated a comparable level of vessel density between the three analyzed groups, suggesting that the above trends in fluorescein accumulation are not due to differences in vessel density but due to BBB permeability (Fig. 4*E*). Likewise, hematoxylin and eosin staining indicated minimal differences

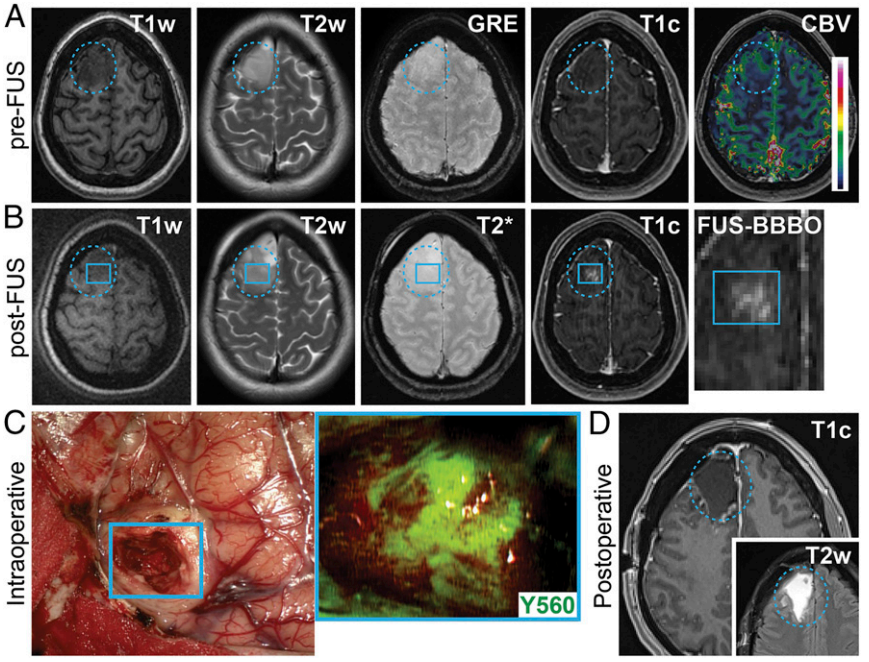

Fig. 2. Targeted BBBO in infiltrating gliomas: (*A*) preoperative axial MR images prior to FUS showing T1w, T2w, GRE, T1c, and cerebral blood volume (CBV) sequences. The blue dotted circle indicates the tumor region. (*B*) Preoperative axial MR images after FUS treatment showing T1w, T2w, GRE/T2*, and T1c sequences. The blue square represents the subspot grid; the inset shows the new contrast enhancement within the target region (e.g., subspot grid). (*C*) Intraoperative white light images showing the earliest stage of tumor surgery during removal of the MB-FUS–targeted region (blue square). Inset shows fluorescence imaging of this region (visualization score = 3) using the Zeiss YELLOW 560 module. (*D*) Postoperative axial T1c and T2w MR images showing resection of the intrinsic tumor.

between MB-FUS–treated and untreated nonenhancing tumor tissues. Together, these findings not only highlight the highly heterogenous permeability of the BBB in infiltrating gliomas but also demonstrate the potential of MB-FUS to improve the delivery and distribution of small-molecular-weight agents in these tumors.

Gradient Echo MRI, Histopathological Analysis of FUS-Treated Regions. To assess the nature of gradient echo (GRE)/T2* changes following MB-FUS BBBO treatments, the MRI-localized surgical specimens were analyzed for evidence of cellular atypia, microhemorrhage, or other cytoarchitectural changes consistent with tissue damage. While there were new GRE/T2* changes within ∼50% of the targeted regions, these regions did not show evidence of tissue damage following surgical removal 2 to 4 h following FUS treatment. Fig. 5 shows the GRE/T2* MRIs for the four patients with varying degrees of new GRE/T2* changes: (*A*) none/minimal, (*B*) significant, (*C*) moderate, and (*D*) none/minimal. The corresponding histological sections of the FUS-treated, and nonenhancing tumor regions of each patient revealed no significant differences and, more specifically, no evidence of microhemorrhages in the MB-FUS–treated regions.

Qualitative and Quantitative Analyses of Acoustic Emissions–Derived HDs and New Contrast-Enhancement and GRE/T2* MRI Changes. With the new capability to assign an AEM level based on subharmonic emissions within a given target region, the relationships between the degree of new contrast-enhancement, the presence of new GRE/T2* changes, and the HD delivered were explored. FUS target regions that received different HDs were compared. Notably, over the course of this study, variations in HDs occurred likely due to differences in tissue characteristics, geometric location of the target(s), and MB concentrations. An example of this is given in Fig. 6 *A* and *B*, in which the target regions in two different patients received HD of 0.5 (patient 3) and 0.8 (patient 1), respectively. Visually, the difference in new contrast-enhancement increased with increasing HD in patients 1, 2, and 3. However, in the current study, it is not possible to separate a putative dose–response relationship within cases from a chance variation in response between cases. Accordingly, these qualitative changes were examined in more detail by tabulating new T1c (Fig. 6*C*) and GRE/T2* (Fig. 6*D*) changes versus the calculated HD in the target region. The T1c and GRE/T2* quantification for patient 4 (treated with software version 7.4) is shown in the insets of Fig. 6 *C* and *D*, respectively. One of the differences between the two software packages is the capability to apply more uniform and more complex shaping of acoustic energy within the target region, accounting for some of the differences observed in the correlations. To account for within-case correlation of MRI signal values, a generalized estimating-equation modeling was conducted. This analysis revealed a statistically significant association between GRE/T2* and HD ($P < 0.01$) and a trend toward significance between new T1c signal and HD ($P = 0.07$). Lastly, the correlations between intraoperative fluorescence visibility and both new T1c changes and HD were evaluated. Similarly, this analysis showed a positive correlation between visible intraoperative fluorescence and these imaging and FUS parameters (*SI Appendix*, Fig. S3). Collectively, these data set the foundation for the development of CFLs during FUS treatments for attaining safe and effective BBBO during MB-FUS in patients with gliomas.

Discussion

Spatial and temporal control of the BBB for treating CNS diseases is a critical frontier in clinical neurosciences. In this study, we report the findings and results from a completed Phase 0 clinical trial in patients with isocitrate dehydrogenase (IDH)-mutant grades II and III infiltrating gliomas undergoing presurgical MRgFUS treatments to study BBBO. Comparative and

Table 1. Patient characteristics of study participants

Mean age at diagnosis – years (age range)	32.5 (29 to 36)
Sex – No. (%)	
Male	3 (75)
Female	1 (25)
KPS – No. (%)	
100	
90	2 (50)
Presenting symptom(s)	2 (50)
Headache	0
Seizure	3
Weakness	0
Incidental (research study volunteer)	1
Mean volume of tumor at diagnosis (cm^3) – No. (range)	18.2 (6.8 to 32.9)
Intrinsic contrast-enhancement No. (%)	2 (50)
Extent of resection at diagnosis (%)	
Gross-total resection	4 (100)
Subtotal resection	0 (0)
Biopsy	0 (0)
WHO histopathological diagnosis (%)	
Diffuse infiltrating glioma (II)	1 (25)
Oligodendroglioma (II)	1 (25)
Anaplastic oligodendroglioma (III)	2 (50)
Anaplastic astrocytoma (III)	0 (0)
Glioblastoma (IV)	0 (0)
IDH mutation status – No. (%)	0 (0)
Nonmutated	4 (100)
Mutated	0 (0)
Unknown	

quantitative analyses were performed based on MRI, histopathological, FUS, AEM, and fluorescence-guided surgery metrics. The MRgFUS system was able to deliver acoustic energy consistently and accurately into the brain and monitor the impact of this energy through AEM. The energy delivery patterns could be conformally shaped to treat specified regions, and the amount of energy within the conformal regions could be monitored and prescribed. There was no evidence of MRI or microscopic tissue injury at ~2 to 4 h following MB-FUS treatment even in the cases in which some new T2*/GRE signal was observed by MRI. A significant and direct correlation was observed between new BBBO in the FUS-targeted regions and the HD delivered into these regions, as calculated from the recorded AEM levels and gauged by gadolinium contrast-enhanced MR imaging. There was also a positive correlation between new BBBO and the intraoperative visualization and histological quantification of fluorescence in the MB-FUS–treated regions. These findings and results demonstrate the safety, feasibility, and potential utility of this emerging technology to control this critical interface within the brain, specifically related to infiltrating gliomas.

The BBB impedes the delivery of most chemotherapies, immunotherapies, nanomedicines, and oncolytic viral vectors, many of which have the potential to treat brain-invading glioma cells and thereby improve outcomes for patients with intrinsic brain tumors such as GBM (9, 31–33). Previous studies suggest that there may be a molecular weight threshold (~2,000 kDa) beyond which some therapeutics do not cross the BBB, even after FUS BBBO (34). In future work, it will be valuable to leverage drug labeling techniques for MR visibility to permit in vivo imaging of biodistribution and trafficking of different types of therapeutic agents. In addition, the ability to control and vary harmonic doses may reveal new information about potential degrees of BBBO and whether such degrees correspond to the passage of molecules of varying molecular weights.

The technology described herein represents a major advancement in the quest to modulate the BBB for therapeutic delivery in brain tumors. The combination of 1) MRI-guidance, 2) computer-controlled beam focusing using multielement transducer arrays, and 3) AEM technologies together offer precision targeting and the potential for CFL control systems. As our

Table 2. Summary of MRgFUS treatment parameters, MB-FUS contrast-enhancement, T2* MRI findings, and intraoperative visualization scoring

Patient	112-001	112-002	112-003	112-004
Time (min)	184	210	173	130
Average power (Watts)	3.38	11.2	11.15	21.55
Volume (cm^3)	0.57	0.57	0.57	10.08
MB dose (mL/dose)	0.34	0.34	0.33	0.35
Normalized T1c (A.U.) (± SD)	0.65 ± 0.03	0.49 ± 0.04	0.34 ± 0.03	0.28 ± 0.05
T2* changes (%) (± SD)	7.17 ± 0.13	3.65 ± 0.22	4.09 ± 0.01	6.03 ± 2.08
Intraoperative visualization	3	ns	1	2

ns: not scored; for patient 112-002 the Zeiss YELLOW 560 module was not available for the surgery.

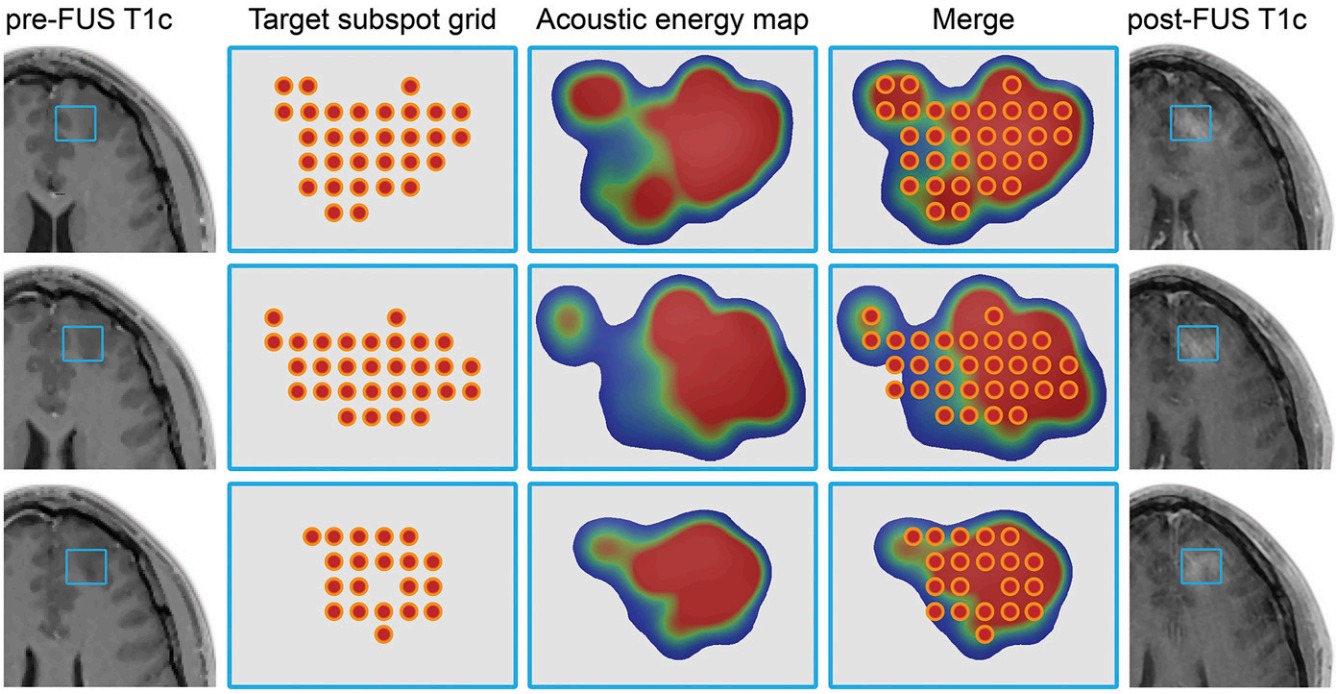

Fig. 3. Target subspot grid, acoustic energy maps, and BBBO: (*Left*) Axial view of T1c MRI acquisitions during treatment planning (pre-FUS). (*Left Middle*) Subspots are positioned across the target subspot grid region during treatment planning. (*Middle*) Following MB-FUS treatment, the accumulated acoustic energy is calculated from the corresponding spectrograms based on AEM data and represented as a colorometric acoustic energy map; note the relative heterogeneity and conformality within the target regions. (*Middle Right*) The intraprocedural view of the subspot grid with underlying energy map showing the real-time deposition of acoustic energy across a given target. (*Right*) The corresponding axial T1c MRI after FUS treatment depicts MB-FUS BBBO.

findings indicated, this technological combination enables safe, highly controlled, and conformal BBBO. The positive correlation, akin to a dose–response curve, between MB-FUS BBBO and the regional HDs observed in this study, demonstrate the degree of control and potential therapeutic utility of this approach. Previous and ongoing studies have explored the safety and feasibility of transcranial (27, 28) and postcraniotomy (14, 15) MB-FUS in glioma patients, demonstrating reproducible, repeated, and/or temporary BBBO in the regions of tumor infiltration. Preclinical studies have set the foundation for AEM monitoring and CFL control to improve further the safety and efficiency of BBBO treatments (20–22, 35). The advancements described here follow on this extensive work by demonstrating its robustness in patients with gliomas and its potential to broaden the applicability of this emerging technology and therapeutic approach in the brain.

The use of AEM to guide and control BBBO is a critical advancement in MB-FUS applications. Huang et al. utilized AEM at the subharmonic spectrum (mean, 115 kHz ± 40) in a preclinical testing on a transhuman skull porcine model to demonstrate consistent detection of transcranial levels as feedback to adjust power levels during treatments establishing a safe threshold for limiting the risk of microhemorrhages (36). Similarly, Tsai et al. demonstrated the use of subharmonic AEM as a control threshold signal to predict safe MB-FUS occurrence (37). In this study and based on this prior work, we incorporated the AEM and harmonic dosing of the subharmonic signal intensities to control for safe acoustic power levels in achieving safe MB-FUS treatments for BBBO.

A missing component in the safety and therapeutic assessments of MB-FUS has been human histopathological studies examining resulting tumor tissue effects and correlating these with observed changes in vascular permeability. We have examined similar tumor regions from each patient, MB-FUS–treated and untreated, and did not uncover evidence of tissue injury or microhemorrhages. Furthermore, we found only a weak correlation between new GRE/T2* signal intensity changes and HDs. A closer look at this data reveals that such a contribution may be attributed to the specific brain regions or, alternatively, could be explained with patient- or tumor-related characteristics. For example, it is entirely possible that some of the T2* changes represent focal areas of localized gadolinium or protein extravasation, which could potentially explain why some of these spots are not visible in follow-up studies (38). While more work and data are needed to better understand the relevance and impact of GRE/T2* signal changes, such data could prove useful in monitoring the effects of MB-FUS in real-time. The current investigation provides evidence that the AEM can be effectively used to minimize adverse effects while attaining effective BBBO.

Localized BBBO could further improve the targeted drug delivery and treatment of diseased brain regions. To investigate this possibility, we analyzed the concentration of fluorescein, a surrogate for an intravenous small molecule drug, in tumor tissues with intrinsic contrast-enhancement, minimal contrast-enhancement, and MB-FUS–mediated contrast-enhancement. This comparison revealed an approximately twofold increase in fluorescein in the FUS-treated compared to untreated nonenhancing tumor tissues. Notably, we observed a positive correlation between MB-FUS HD, intraoperative visibility score, and measured intratumoral fluorescein. This represents a quantitative measurement in humans of the drug delivery potential of MB-FUS based on AEM-controlled harmonic dosing. Numerous preclinical studies have included similar comparisons showing three- to fivefold increases in FUS-treated versus untreated brain and tumor tissues (20, 24, 39, 40). A previous clinical study tabulated data for one patient treated with liposomal doxorubicin and another patient treated with temozolomide in sonicated versus nonsonicated tumor tissues. The data were given in low concentrations (ng/mL) and without statistical data to support the potential impact of FUS BBBO on therapeutic delivery (28). Other time-course studies have focused on post-FUS effects,

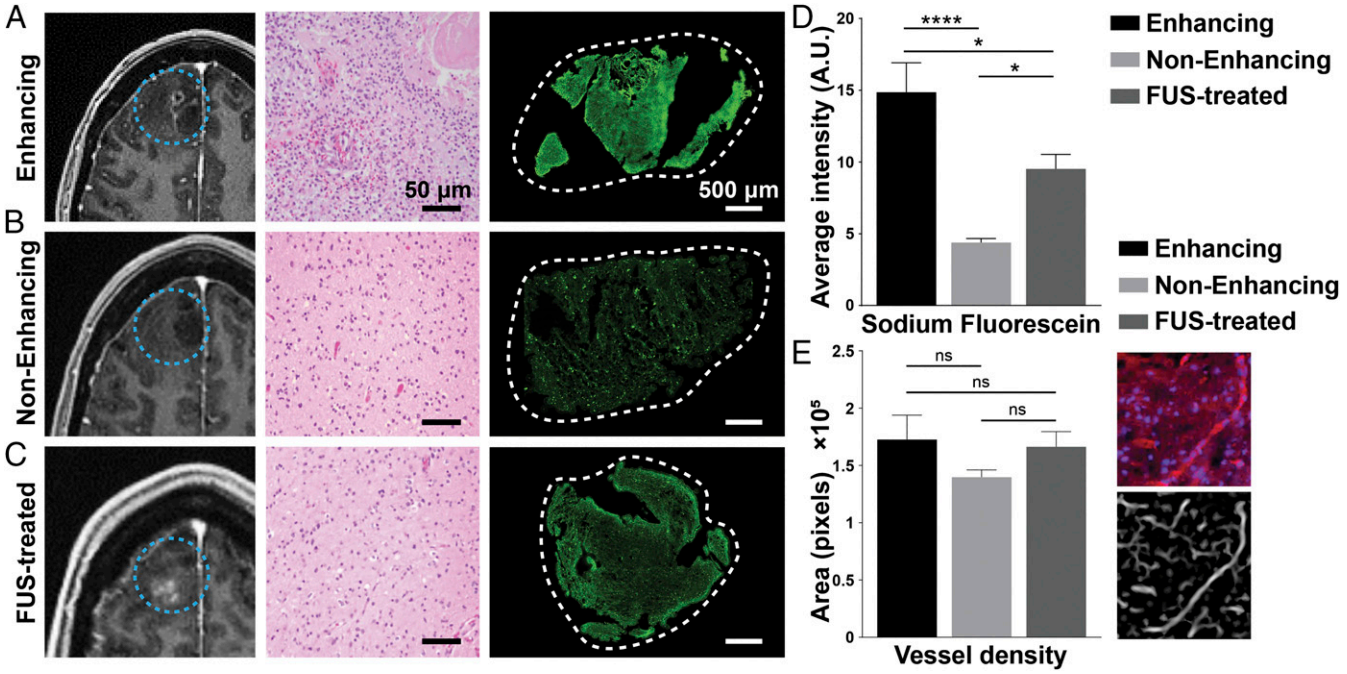

Fig. 4. MRI, histology, and fluorescein intensity of intrinsically enhancing, nonenhancing, and FUS-treated tumor regions. (*A–C*) Preoperative contrast-enhanced T1w MRI (*Left*) in axial view showing intrinsically enhancing, nonenhancing, and FUS-treated glioma regions, respectively (blue dotted circle). Representative histologic hematoxylin and eosin slices (*Middle*) from resected tissues are shown next to the MRI images. (Scale bar, 50 μm.) Fluorescein accumulation in the tissue (*Right*) imaged with a 20× objective at excitation wavelengths of 488 nm. (*D*) Quantification of sodium fluorescein intensity for intrinsically enhancing, nonenhancing, and FUS-treated glioma regions indicated in arbitrary units (A.U.). (*E*) Quantification of vessel density in tissue samples resected from intrinsically enhancing, nonenhancing, and FUS-treated glioma regions. Immunofluorescence staining of a vascular marker (CD31, red) and cell nucleus (DAPI, blue) was imaged with a 20× objective at excitation wavelengths of 405 nm and 561 nm for CD31 and DAPI, respectively. We assessed vessel density in the same region by using ImageJ's tubeness function. Plots show means ± SEM ($n = 4$). *P* values were determined by unpaired *t* tests (*$P \leq 0.01$; ****$P \leq 0.0001$).

revealing that both microglia and astrocyte activation resolved within 15 d with no evidence of glial scar or reactive astrocytosis, thereby suggesting that FUS treatment did not cause prolonged reactive changes or gliosis (41–44). Our investigations assess the potency of MB-FUS in BBBO in humans while accounting for critical tumor microenvironment parameters including BBB leakiness and vascular density.

The use of intravascular dyes to mark operative targets and enable fluorescence-guided surgery is increasingly used to improve the safety and efficacy of cancer surgery (45–48). Recently, numerous groups have reported the value of sodium fluorescein–enhanced brain tumor surgery to not only reveal but also demarcate contrast-enhancing tumor tissues. Nevertheless, in certain brain tumor types, the most common being infiltrating gliomas, there are often tumor components with no or limited intrinsic contrast-enhancement (Fig. 4). In some cases, the entire tumor is nonenhancing, making it challenging to distinguish the infiltrated from the adjacent brain parenchyma (5). There is a growing appreciation for the prognostic value of nonenhancing tumor regions in GBM. Extending neurosurgical resection beyond the contrast-enhancing tumor to the nonenhancing peritumoral component has been associated with improved survival (49). Accordingly, a method that increases the degree of contrast-enhancement within a planned surgical resection volume offers the potential to improve intraoperative visibility using fluorescein-based (or similar visible dye) techniques. The results from this study suggest that 1) fluorescein is delivered into MB-FUS–treated tumor tissues in an HD-dependent fashion, 2) the blood–brain/tumor barrier remains open for at least 2 to 4 h after MB-FUS, and 3) fluorescein can mark FUS-treated regions. It should be noted that the timing of fluorescein administration may impact tissue fluorescence and related visibility due to the balance between dye extravasation and interstitial clearance, as well as leakage from other cut or leaky vessels within the surgical field (50). Further research in assessing the required dose, method, and timing of fluorescein delivery, beyond what was used in this study that followed those commonly used in neurosurgical practice as described in other studies and institutional protocols (51, 52), is warranted.

Presurgical MB-FUS BBBO not only offers the opportunity to study brain and tumor tissues post-FUS with the potential for enhanced intraoperative visibility during tumor resections but also establishes a paradigm to test FUS-therapeutic combinations (53). In this way, the change in plasma to tissue concentrations of various promising therapeutics in sonicated versus nonsonicated regions of a tumor can be assessed. This enables close examination of differences with and without MB-FUS, between patients, and within a given tumor. Such early-phase window-of-opportunity studies could accelerate the selection of FUS-therapeutic combinations for larger-scale safety and efficacy clinical trials.

The development and application of transcranial FUS systems for the treatment of brain disorders is rapidly accelerating. This emerging treatment modality offers new, effective, and noninvasive approaches to intervene in essential tremor, Parkinson's disease, Alzheimer's disease, psychiatric disorders, chronic pain conditions, brain tumors, and likely many more indications in the near future (10). The speed of technological advancement of clinical FUS systems has, in some ways, outpaced the development of similar systems for representative preclinical modeling and examinations of clinical treatments. Notably, this also includes the study of thermo- and mechanobiology of FUS effects in the CNS and other tissues. Experimental systems that enable or include the study of biological responses to FUS will help guide the clinical translation of FUS-based treatments, in particular, combination therapies. An important example of this

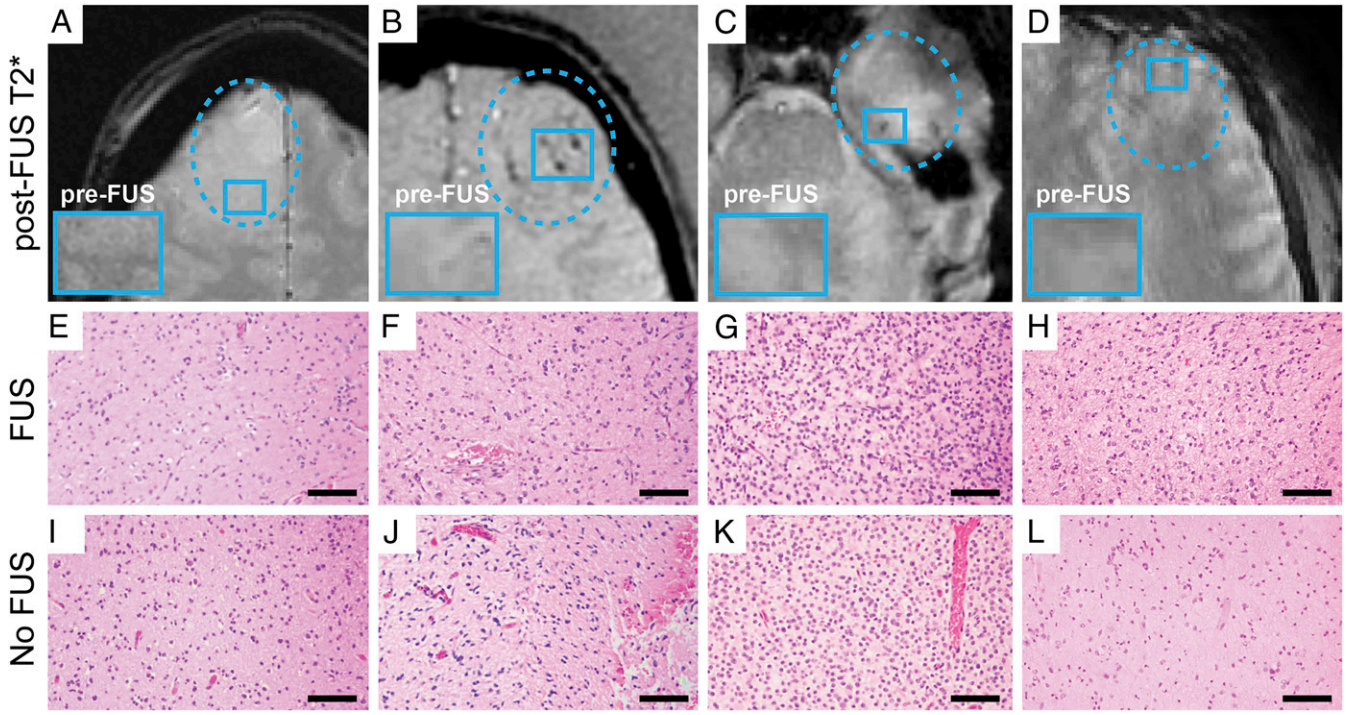

Fig. 5. Post-FUS T2* changes and correlation with surgical pathology. GRE MRIs for the four study participants with varying degrees of new T2* changes: (*A*) none/minimal, (*B*) significant, (*C*) moderate, and (*D*) none/minimal. The corresponding hematoxylin and eosin–stained histological sections of the (*E–H*) FUS-treated (FUS) and (*I–L*) untreated nonenhancing (No FUS) tumor regions for each of the four patients revealed no significant differences and, more specifically, no evidence of microhemorrhages in the FUS-treated regions. (Scale bar, 50 μm.)

idea is the possibility that the mechanobiological effects of MB-FUS may also alter the immune microenvironment within treated tissues and offer unique opportunities for immunomodulation and enhancement of immunotherapies (54–56). This possibility could be an important consideration in ongoing and planned clinical trials with MB-FUS chemotherapy combinations (NCT03551249, NCT04417088, and NCT04528680). While this work is based on a small, early-phase clinical trial, the results serve to propel MRgFUS for applications in infiltrating gliomas, highlight the opportunity to leverage harmonic dosing and CFLs in MB-FUS treatments, and demonstrate a unique strategy for highly controlled and conformal BBBO.

While this study offers numerous findings and technological considerations related to MB-FUS, there are some notable limitations. First, the data and results derive from a small study cohort, and the first three patients were treated using ExAblate Neuro interface 7.0. This early version of the computer interface was limited in the subspot targeting array design to nine total subspots within a square grid. As the control systems advanced over the course of the study, the ExAblate Neuro was upgraded to interface 7.4, which created a much higher degree of flexibility in subspot number and design. Second, in the process of brain surgery, the dura is opened and the cerebrospinal fluid within is inevitably released. This process can lead to a spatial shift in the brain compared to the surgical neuronavigation system, which is based on the presurgical geometry and used for stereotactic localization. This potential shift could have introduced error in the localization of the MB-FUS target region following dural opening. In order to reduce the potential impact of this error, the study design included only lobar tumor locations in which relatively superficial tumor locations could be targeted for MB-FUS treatment. In this way, the MB-FUS–treated region was encountered early in the surgery and prior to substantial brain shift, which generally increases over the course of tumor resection. Lastly, the study cohort had mainly young patients with IDH-mutated tumors. These cohort characteristics limit the generalizability of the study findings. Future work is warranted to expand this application of MB-FUS for both surgical marking of gliomas to guide surgical resection as well as to test MB-FUS drug combinations for enhanced delivery and early signs of therapeutic efficacy.

Materials and Methods

Study Design and Protocol. In this single-arm, nonrandomized, open-label feasibility study, we aimed to evaluate the safety and feasibility of focal BBBO in patients diagnosed with intrinsic brain tumors. All study participants were referred to neurosurgical service after initial imaging diagnosis of suspected infiltrating glioma. A complete list of inclusion and exclusion criteria can be found in *SI Appendix*, Table S1. Informed consent for surgical resection and research participation was obtained. The study protocol was approved by the FDA for enrollment of five cases in a Phase 0 feasibility and early safety trial as well as by the Institutional Review Board of the University of Maryland School of Medicine and registered with ClinicalTrials.gov (NCT03322813). Representatives of the InSightec's ExAblate Neuro Type 2 MRgFUS system used for the BBBO treatments provided technical support during the course of the trial.

MRI Parameters. T1-weighted (T1w), T2-weighted (T2w), and T2*-weighted (T2*) MRI sequences were acquired presonication for baseline and treatment planning. T1w sequences were obtained before and after gadolinium administration (T1c). Baseline MR scans were obtained on either the 1.5T Magnetom Avanto (Siemens Healthineers) or the 3.0T 750W Discovery (GE Healthcare) MRI scanner. MRI scans during the BBBO procedure and post-BBBO were obtained using the 3.0T 750W Discovery Scanner.

For the Siemens 1.5T Avanto system, MRI scans included axial T1w magnetization prepared rapid acquisition gradient echo sequences (repetition time [TR]: 1,800 to 2,200 ms; echo time [TE]: 3.02 to 3.37 ms; Flip Angle: 8 to 15°), axial T1w spin-echo (SE) sequences (TR: 400 ms; TE: 8.9 ms; Flip Angle: 90°), axial susceptibility-weighted imaging sequences (TR: 49 ms; TE: 40 ms; Flip Angle: 15°), and axial T2w SE sequences (TR: 4510 ms; TE: 88 ms; Flip Angle: 150°).

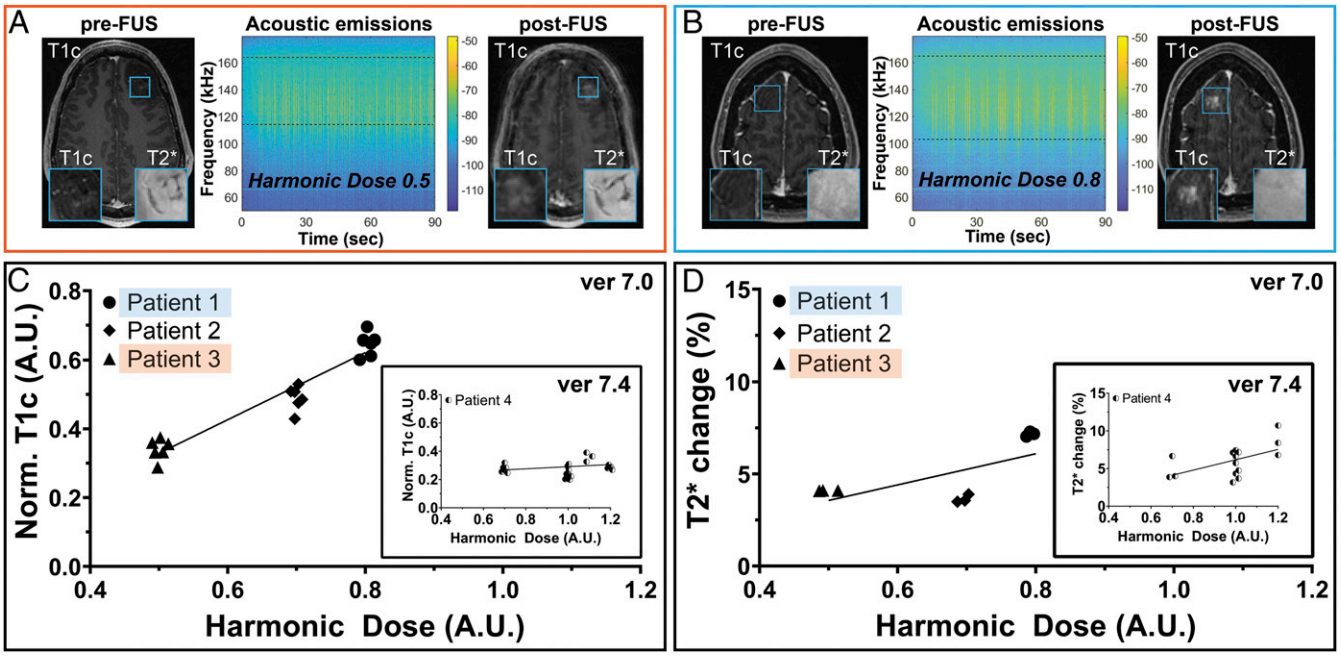

Fig. 6. Acoustic emissions and HD correlations with MRI findings: (*A* and *B*) T1c and GRE/T2* axial MR images before (*Left*) and after (*Right*) FUS treatment reveal differences in new vascular permeability corresponding to BBBO accompanied by minimal changes in interstitial components, respectively. Insets show magnified T1c (*Lower Left*) and GRE/T2* (*Lower Right*) of the target region indicated by the blue square in the respective MR images. The corresponding spectrograms (*Center*) and HDs calculated from these spectrograms of 0.5 (patient 3, red box) and 0.8 (patient 1, blue box) show levels correlating with the degree of new T1c. The HD per subspot was calculated as the accumulated harmonic score (over all pulses/sonications) divided by the number of subspots. These values are unitless, as they are referenced against a calibration value. (*C* and *D*) To account for within-case correlation of MRI signal values, a generalized estimating-equation modeling was conducted. This analysis revealed a statistically significant association between GRE/T2* and HD ($P < 0.001$) but not between the new T1c signal and HD ($P = 0.07$). The insets show the quantification of the corresponding T1c and T2* values for patient 4, respectively. Notably, patients 1, 2, and 3 were treated using ExAblate Neuro's interface version 7.0, while patient 4 was treated using ExAblate Neuro's interface version 7.4, which allowed coverage of more complex shaped target grids of up to 32 subspots as well as more uniform energy distribution within a given target grid. Patient 4 was treated at four different HDs. The treatment of HD at 1.1 was not included due to moving artifacts in the MRI acquisitions (MRI data are given in arbitrary units of voxel intensity).

For the GE 3.0T 750W Discovery, MRI scans included axial T1w fast spoiled gradient-echo sequences (TR: 8.64 to 8.66 ms; TE: 3.21 ms; Flip Angle: 12°), axial T2w fast spin-echo sequences (TR: 5,814 to 6,012 ms; TE: 103.58 to 103.87 ms; Flip Angle: 142°), axial T2 fluid-attenuated inversion recovery sequences (TR: 9,000 ms; TE: 96.10 ms; Flip Angle: 160°), and axial T2* (TR: 317 ms; TE: 15 ms; Flip Angle: 20°).

Gadavist gadolinium-based contrast agent (Bayer Healthcare) was administered intravenously following a standard weight-based dose of 0.1 mmol per kilogram of body weight. All MRI scans were jointly reviewed by the neurosurgeon and neuroradiologist.

FUS BBBO and Tumor Resection. The ExAblate Neuro 2 (InSightec) MRgFUS system was used for transcranial FUS treatments. Following a complete head shave, an MRI-certified stereotactic head frame was positioned and secured on the patient's head prior to placing the patient inside the MRI in a supine position. The headframe was then coupled with a hemispherical helmet-shaped phased array containing 1,024 individually steerable transducers. The ExAblate Neuro 2 system operates at a center frequency of 230 kHz. During treatment planning, T1w and T2w MRI scans were performed using a 3.0T head coil (Model: GEM HNU; REF 5445051, GE Healthcare Coils). Stereotactic targeting was performed after coregistration of the CT and MR acquisitions. The sonication volume was delineated by a volumetric subspot lattice with 3-mm spacing between individual subspots. This earlier version of the software (version 7.0) was utilized for the first three patients (patients 1, 2, and 3) allowing targeting of a 3×3 subspot grid to cover ~0.567 cm^3 target brain volume. The ExAblate Neuro 2's software system underwent an upgrade allowing for the design of user-defined complex geographical regions during treatment planning. The subsequent software upgrade to 7.4 allowed coverage of more complex, shaped target grids of up to 32 subspots as well as more uniform energy distribution within a given target grid. Several target volumes could be targeted after each MB injection as long as MB activity was detected by the system's AEM system (e.g., hydrophones).

The AEM system records the cavitation score for each pulse during sonications by utilizing the hydrophones integrated into the hemispherical array. For each single hydrophone, the mean root square voltage detected by the appropriate circuitry within a band centered around half the center frequency of the system (230 kHz) is recorded. The HD is calculated as the accumulated score over all pulses divided by the number of subspots in a given region and averaged over all hydrophones. The resulting values are unitless, as they are referenced against a calibration value.

Immediately preceding sonications, the patients received an intravenous bolus injection of DEFINITY (Lantheus Medical Imaging, Inc.) MBs at 4 to 5 μL per kilogram body weight per injection. The total dose of DEFINITY did not exceed 20 μL/kg. Acoustic energy was sequentially titrated using a ramp-up function approach. Each brief sonication was informed by real-time AEM facilitated by an array of eight hydrophones integrated into the acoustic helmet. Optimal power for BBBO was calculated as 50% of the power at which cavitation signals were recorded using a real-time acoustic emissions feedback system. The optimal power threshold was determined by incrementally increasing the power at short intervals of 5% until a subharmonic signal could be detected, at which point only 50% of that given power level was applied to the subsequent sonications. This power ramping process was performed once per target for each patient. It should also be noted that the power threshold varied only marginally between neighboring subspots.

Sonications were delivered at 8% duty cycle (the percentage of time the transducers are activated) over 90-s intervals during which the acoustic beam was steered by the system from the initial subspot sequentially through each subsequent subspot in a linear recycling pattern (Fig. 1*B*). Patients were intermittently assessed for any new symptoms or neurologic signs. Contrast-enhanced T1w MRI sequences were acquired immediately after completion of sonications to confirm BBBO. T2* MRI sequences were used to assess for possible microhemorrhage. Following the MRgFUS procedure, patients were directly transported to the operating room and prepared for surgery and tumor resection.

Patients were intubated and underwent general anesthesia. They were pinned in a Mayfield frame, and their imaging was registered with a BrainLab navigation system (BrainLab). Standard craniotomies were performed depending on lesion location (e.g., frontal or pterional). Sodium fluorescein was administered intravenously at a dose of 3 mg per kilogram of body weight immediately after the surgical incision was made. Using gadolinium-enhanced BrainLab neuronavigation, contrast-enhancing (when present), nonenhancing, and fluorescein-enhancing samples were stereotactically localized and resected for further analysis. These were performed using brightfield and fluorescent microscopy using the KINEVO 900 (Carl Zeiss). After surgery, patients were extubating and transported to the neurological intensive care unit for postoperative care. Brain tumor tissue was resected during surgery from three different brain regions: FUS-treated, intrinsically enhancing, and nonenhancing. Tissue samples were sliced, mounted on glass slides, and prepared for immunofluorescence analysis. The BBBO, as defined by contrast-enhancement per subspot region, was numerically quantified using a script implemented in MATLAB version R2019b (MathWorks, Inc.). One neurosurgeon (G.F.W.) performed the surgery for all four cases in this study.

Fluorescein Analysis of Brain Tumor Tissues. Resected brain tumor tissues removed from the four trial participants during surgery were embedded in optimal cutting temperature compound and stored frozen at −80 °C. Tissues from intrinsically enhancing, nonenhancing, and FUS-treated regions of interest (ROIs) were subsequently sectioned at 20-μm thickness and mounted onto microscopy slides. Tissue slices from the three ROIs were initially imaged using epifluorescence microscopy to evaluate the biodistribution of sodium fluorescein. Next, tissues were prepared for immunofluorescence staining using CD31 as a marker to assess blood vessel density.

Fresh-frozen tissue slices were fixed for 10 min at room temperature with 4% paraformaldehyde (Electron Microscopy Sciences). After two serial washes with phosphate-buffered saline (PBS), the sections were blocked for 1 h with 2% bovine serum albumin (Sigma-Aldrich) and 5% goat serum (Thermo Fisher Scientific) in PBS solution at room temperature, followed by a 12-h incubation at 4 °C with primary antibody. CD31 rabbit anti-human primary antibody was used at a 1:100 dilution (Abcam). Following exposure to the primary antibody, the tissues were incubated with the secondary antibody for 1 h at room temperature. Donkey anti-rabbit conjugated to Alexa Fluor 555 was used at a 1:250 dilution (Thermo Fisher Scientific). The sections were then mounted with Prolong Glass Antifade Mountant (Thermo Fisher Scientific), covered with coverslips, and allowed to cure for 24 h in the dark at room temperature prior to imaging.

All images were acquired using the LSM 780/ ELYRA PS1 confocal laser microscope (Carl Zeiss) with a 20× objective at excitation wavelengths of 488 nm and 561 nm for sodium fluorescein and CD31, respectively. To quantify the sodium fluorescein intensity in the tumor, the confocal images were processed using a custom-developed MATLAB script using Matlab 2019a (MathWorks, Inc.). In brief, the script determined the tumor ROI by applying an edge-detection method so that the measured average fluorescein intensity was emanated from within the tumor. To quantify vascular density within the tumor tissues, we scored curvilinearity using the ImageJ plugin "tubeness" bundled with Fiji (57). The tubeness plugin performs a Gaussian smoothing of the image being analyzed, followed by multiplying the two lowest eigenvalues of the local Hessian matrix. High tubeness scores are assigned when two eigenvalues are negative and zero otherwise. The tubeness scores were then thresholded to generate a binary image to capture the vascular patterns and assign a measure of tubeness to each pixel within the image (58). Each data set (intrinsically enhancing, nonenhancing, and FUS-treated) was processed and analyzed using identical processing steps and parameters. The intraoperative visualization of fluorescence using the Zeiss YELLOW 560 module (OPMI Pentero, Carl Zeiss) was graded by the neurosurgeon. Using stereotactic localization early in the tumor resection, the FUS-treated target region was inspected. The grades were given as clear visualization (score = 3), moderate visualization (score = 2), minimal visualization (score = 1), or no visualization (score = 0). These results were tabulated and displayed against the calculated harmonic dose and new contrast-enhancement in Table 2 and *SI Appendix*, Fig. S3.

Assessment of New Contrast-Enhancement. The BBBO as defined by contrast-enhancement within the FUS-targeted region was analyzed using a multimodal algorithmic approach implemented in MATLAB version R2019b (MathWorks, Inc.). In brief, the script converted the MRI Digital Imaging and Communications in Medicine (DICOM) sequences into isometric tagged image file format (TIFF) slices. All slices, including pre- and post-FUS, were coregistered to the same Cartesian coordinate system in the three-dimensional space. Next, we realized a skull extraction algorithm followed by an intensity-based normalization. The analysis was performed in a semiautomated fashion with user input required to define the area of treatment and the internal standards to which pixel intensities were normalized. Internal standards used for normalization were the ocular muscles (ipsi- and contralateral), the posterior pituitary gland, and the choroid plexi (ipsi- and contralateral) on both the pre- and post-FUS contrast-enhanced MRI slices.

Statistical Analysis. For the fluorescein analysis, P values were determined using the unpaired two-tailed Student's t test with values of $P < 0.05$ considered significant. The association between both T1c and HD and GRE/T2* and HD were tested using generalized estimating-equation modeling assuming a normal distribution of MRI values around the mean, and identity as the link function was conducted to test for an association of these parameters with HD while adjusting for the intrapatient correlation arising from the multiple sampling within cases. Statistical analyses were conducted in IBM SPSS release 27.0.0 (released 2020: IBM Corp).

Data Availability. All study data are included in the article and/or *SI Appendix*.

ACKNOWLEDGMENTS. This clinical trial was sponsored by InSightec, Inc. We acknowledge the following individuals from InSightec, who were essential to the performance of this study: Rafi De Picciotto, Ryan Clanton, Nathaniel Kelm, Kathy McDermott, and Nadir Alikacem. We would also like to acknowledge the support provided by Lantheus Medical Imaging, Inc. in supplying DEFINITY microbubbles for this clinical trial. P.A. was supported by the Cancer Biology Training Grant NIH 5T32CA154274. C.A. and Y.G. were supported by the NIH Grant R37CA239039. G.F.W. was supported by the Focused Ultrasound Foundation Andrew J. Lockhart Memorial Award.

1. C. H. Lai, K. H. Kuo, The critical component to establish in vitro BBB model: Pericyte. *Brain Res. Brain Res. Rev.* **50**, 258–265 (2005).
2. A. Lalatsa, A. M. Butt, "Physiology of the blood-brain barrier and mechanisms of transport across the BBB" in *Nanotechnology-Based Targeted Drug Delivery Systems for Brain Tumors*, P. Kesharwani, U. Gupta, Eds. (Academic Press, 2018), pp. 49–74.
3. C. D. Arvanitis, G. B. Ferraro, R. K. Jain, The blood-brain barrier and blood-tumour barrier in brain tumours and metastases. *Nat. Rev. Cancer* (2019).
4. O. van Tellingen *et al*., Overcoming the blood-brain tumor barrier for effective glioblastoma treatment. *Drug Resist. Updat.* **19**, 1–12 (2015).
5. J. N. Sarkaria *et al*., Is the blood-brain barrier really disrupted in all glioblastomas? A critical assessment of existing clinical data. *Neuro. Oncol.* **20**, 184–191 (2018).
6. W. M. Pardridge, The blood-brain barrier: Bottleneck in brain drug development. *NeuroRx.* **2**, 3–14 (2005).
7. B. Obermeier, R. Daneman, R. M. Ransohoff, Development, maintenance and disruption of the blood-brain barrier. *Nat. Med.* **19**, 1584–1596 (2013).
8. A. E. Caprifico, P. J. S. Foot, E. Polycarpou, G. Calabrese, Overcoming the blood-brain barrier: Functionalised chitosan nanocarriers. *Pharmaceutics* **12**, 1013–1033 (2020).
9. R. Haumann, J. C. Videira, G. J. L. Kaspers, D. G. van Vuurden, E. Hulleman, Overview of current drug delivery methods across the blood-brain barrier for the treatment of primary brain tumors. *CNS Drugs* **34**, 1121–1131 (2020).
10. Y. Meng, K. Hynynen, N. Lipsman, Applications of focused ultrasound in the brain: From thermoablation to drug delivery. *Nat. Rev. Neurol.* **17**, 7–22 (2021).
11. P. Ghanouni *et al*., Transcranial MR-guided focused ultrasound: A review of the technology and neuro applications. *AJR Am. J. Roentgenol.* **205**, 150–159 (2015).
12. W. Y. Chai *et al*., Image-guided focused-ultrasound CNS molecular delivery: An implementation via dynamic contrast-enhanced magnetic-resonance imaging. *Sci. Rep.* **8**, 4151 (2018).
13. S. K. Wu *et al*., Characterization of different microbubbles in assisting focused ultrasound-induced blood-brain barrier opening. *Sci. Rep.* **7**, 46689 (2017).
14. A. Carpentier *et al*., Clinical trial of blood-brain barrier disruption by pulsed ultrasound. *Sci. Transl. Med.* **8**, 343re2 (2016).
15. A. Idbaih *et al*., Safety and feasibility of repeated and transient blood-brain barrier disruption by pulsed ultrasound in patients with recurrent glioblastoma. *Clin. Cancer Res.* **25**, 3793–3801 (2019).
16. W. J. Elias *et al*., A Randomized trial of focused ultrasound thalamotomy for essential tremor. *N. Engl. J. Med.* **375**, 730–739 (2016).
17. T. Sun *et al*., Closed-loop control of targeted ultrasound drug delivery across the blood-brain/tumor barriers in a rat glioma model. *Proc. Natl. Acad. Sci. U.S.A.* **114**, E10281–E10290 (2017).
18. M. Çavuşoğlu *et al*., Closed-loop cavitation control for focused ultrasound-mediated blood-brain barrier opening by long-circulating microbubbles. *Phys. Med. Biol.* **64**, 045012 (2019).
19. B. Cheng, C. Bing, R. Chopra, The effect of transcranial focused ultrasound target location on the acoustic feedback control performance during blood-brain barrier opening with nanobubbles. *Sci. Rep.* **9**, 20020–20020 (2019).
20. N. McDannold *et al*., Acoustic feedback enables safe and reliable carboplatin delivery across the blood-brain barrier with a clinical focused ultrasound system and improves survival in a rat glioma model. *Theranostics* **9**, 6284–6299 (2019).

21. M. A. O'Reilly, K. Hynynen, Blood-brain barrier: Real-time feedback-controlled focused ultrasound disruption by using an acoustic emissions-based controller. *Radiology* **263**, 96–106 (2012).
22. A. Patel, S. J. Schoen Jr, C. D. Arvanitis, Closed loop spatial and temporal control of cavitation activity with passive acoustic mapping. *IEEE Trans. Biomed. Eng.*, 10.1109/TBME.2018.2882337 (2018).
23. C. D. Arvanitis, M. S. Livingstone, N. Vykhodtseva, N. McDannold, Controlled ultrasound-induced blood-brain barrier disruption using passive acoustic emissions monitoring. *PLoS One* **7**, e45783 (2012).
24. M. Aryal, C. D. Arvanitis, P. M. Alexander, N. McDannold, Ultrasound-mediated blood-brain barrier disruption for targeted drug delivery in the central nervous system. *Adv. Drug Deliv. Rev.* **72**, 94–109 (2014).
25. N. Lipsman *et al*., Blood-brain barrier opening in Alzheimer's disease using MR-guided focused ultrasound. *Nat. Commun.* **9**, 2336 (2018).
26. A. R. Rezai *et al*., Noninvasive hippocampal blood-brain barrier opening in Alzheimer's disease with focused ultrasound. *Proc. Natl. Acad. Sci. U.S.A.* **117**, 9180–9182 (2020).
27. S. H. Park *et al*., Safety and feasibility of multiple blood-brain barrier disruptions for the treatment of glioblastoma in patients undergoing standard adjuvant chemotherapy. *J. Neurosurg.*, 10.3171/2019.10.JNS192206. (2020).
28. T. Mainprize *et al*., Blood-brain barrier opening in primary brain tumors with non-invasive MR-guided focused ultrasound: A clinical safety and feasibility study. *Sci. Rep.* **9**, 321 (2019).
29. P. A. Dayton, K. W. Ferrara, Targeted imaging using ultrasound. *J. Magn. Reson. Imaging* **16**, 362–377 (2002).
30. G. E. Weller *et al*., Ultrasonic imaging of tumor angiogenesis using contrast microbubbles targeted via the tumor-binding peptide arginine-arginine-leucine. *Cancer Res.* **65**, 533–539 (2005).
31. M. S. Soto, N. R. Sibson, The multifarious role of microglia in brain metastasis. *Front. Cell. Neurosci.* **12**, 414 (2018).
32. W. M. Pardridge, CSF, blood-brain barrier, and brain drug delivery. *Expert Opin. Drug Deliv.* **13**, 963–975 (2016).
33. W. A. Banks, From blood-brain barrier to blood-brain interface: New opportunities for CNS drug delivery. *Nat. Rev. Drug Discov.* **15**, 275–292 (2016).
34. J. J. Choi, S. Wang, Y.-S. Tung, B. Morrison III, E. E. Konofagou, Molecules of various pharmacologically-relevant sizes can cross the ultrasound-induced blood-brain barrier opening in vivo. *Ultrasound Med. Biol.* **36**, 58–67 (2010).
35. H. A. Kamimura *et al*., Feedback control of microbubble cavitation for ultrasound-mediated blood-brain barrier disruption in non-human primates under magnetic resonance guidance. *J. Cereb. Blood Flow Metab.* **39**, 1191–1203 (2019).
36. Y. Huang, R. Alkins, M. L. Schwartz, K. Hynynen, Opening the blood-brain barrier with MR imaging-guided focused ultrasound: Preclinical testing on a trans-human skull porcine model. *Radiology* **282**, 123–130 (2017).
37. C. H. Tsai, J. W. Zhang, Y. Y. Liao, H. L. Liu, Real-time monitoring of focused ultrasound blood-brain barrier opening via subharmonic acoustic emission detection: Implementation of confocal dual-frequency piezoelectric transducers. *Phys. Med. Biol.* **61**, 2926–2946 (2016).
38. M. El-Koussy *et al*., Susceptibility-weighted imaging of the brain: Does gadolinium administration matter? *Eur. J. Radiol.* **81**, 272–276 (2012).
39. E. L. Yuh *et al*., Delivery of systemic chemotherapeutic agent to tumors by using focused ultrasound: Study in a murine model. *Radiology* **234**, 431–437 (2005).
40. L. Goldwirt *et al*., Enhanced brain distribution of carboplatin in a primate model after blood-brain barrier disruption using an implantable ultrasound device. *Cancer Chemother. Pharmacol.* **77**, 211–216 (2016).
41. J. Silburt, N. Lipsman, I. Aubert, Disrupting the blood-brain barrier with focused ultrasound: Perspectives on inflammation and regeneration. *Proc. Natl. Acad. Sci. U.S.A.* **114**, E6735–E6736 (2017).
42. M. Pekny, M. Pekna, Astrocyte reactivity and reactive astrogliosis: Costs and benefits. *Physiol. Rev.* **94**, 1077–1098 (2014).
43. T. Scarcelli *et al*., Stimulation of hippocampal neurogenesis by transcranial focused ultrasound and microbubbles in adult mice. *Brain Stimul.* **7**, 304–307 (2014).
44. J. F. Jordão *et al*., Amyloid-β plaque reduction, endogenous antibody delivery and glial activation by brain-targeted, transcranial focused ultrasound. *Exp. Neurol.* **248**, 16–29 (2013).
45. E. Belykh *et al*., Blood-brain barrier, blood-brain tumor barrier, and fluorescence-guided neurosurgical oncology: Delivering optical labels to brain tumors. *Front. Oncol.* **10**, 739 (2020).
46. W. Stummer *et al*.; ALA-Glioma Study Group, Fluorescence-guided surgery with 5-aminolevulinic acid for resection of malignant glioma: A randomised controlled multicentre phase III trial. *Lancet Oncol.* **7**, 392–401 (2006).
47. Q. T. Nguyen, R. Y. Tsien, Fluorescence-guided surgery with live molecular navigation—A new cutting edge. *Nat. Rev. Cancer* **13**, 653–662 (2013).
48. L. J. Lauwerends *et al*., Real-time fluorescence imaging in intraoperative decision making for cancer surgery. *Lancet Oncol.* **22**, e186–e195 (2021).
49. A. Lasocki, F. Gaillard, Non-contrast-enhancing tumor: A new frontier in glioblastoma research. *AJNR Am. J. Neuroradiol.* **40**, 758–765 (2019).
50. W. Stummer, Factors confounding fluorescein-guided malignant glioma resections: Edema bulk flow, dose, timing, and now: Imaging hardware? *Acta Neurochir. (Wien)* **158**, 327–328 (2016).
51. F. Acerbi *et al*., Fluorescein-guided surgery for resection of high-grade gliomas: A multicentric prospective phase II study (FLUOGLIO). *Clin. Cancer Res.* **24**, 52–61 (2018).
52. R. Rey-Dios, A. A. Cohen-Gadol, Technical principles and neurosurgical applications of fluorescein fluorescence using a microscope-integrated fluorescence module. *Acta Neurochir. (Wien)* **155**, 701–706 (2013).
53. B. Glimelius, M. Lahn, Window-of-opportunity trials to evaluate clinical activity of new molecular entities in oncology. *Ann. Oncol.* **22**, 1717–1725 (2011).
54. K. Beccaria *et al*., Blood-brain barrier opening with low intensity pulsed ultrasound for immune modulation and immune therapeutic delivery to CNS tumors. *J. Neurooncol.* **151**, 65–73 (2020).
55. C. T. Curley, N. D. Sheybani, T. N. Bullock, R. J. Price, Focused ultrasound immunotherapy for central nervous system pathologies: Challenges and opportunities. *Theranostics* **7**, 3608–3623 (2017).
56. K.-T. Chen *et al*., Neuronavigation-guided focused ultrasound for transcranial blood-brain barrier opening and immunostimulation in brain tumors. *Sci. Adv.* **7**, eabd0772 (2021).
57. J. Schindelin *et al*., Fiji: An open-source platform for biological-image analysis. *Nat. Methods* **9**, 676–682 (2012).
58. Y. Sato *et al*., Three-dimensional multi-scale line filter for segmentation and visualization of curvilinear structures in medical images. *Med. Image Anal.* **2**, 143–168 (1998).